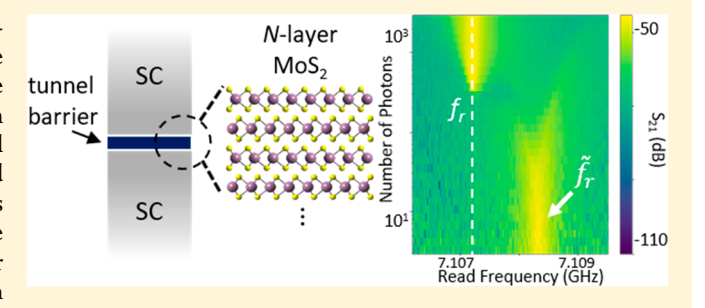
# Two-Dimensional Material Tunnel Barrier for Josephson Junctions and Superconducting Qubits

Kan-Heng Lee,  $^{\dagger,\ddagger_{0}}$  Srivatsan Chakram,  $^{\$,\#}$  Shi En Kim,  $^{\ddagger}$  Fauzia Mujid,  $^{\parallel}$  Ariana Ray,  $^{\dagger}$  Hui Gao,  $^{\perp,\parallel}$  Chibeom Park,  $^{\$,\parallel}$  Yu Zhong,  $^{\parallel}$  David A. Muller,  $^{\dagger}$  David I. Schuster,  $^{*,\ddagger,\$,\#}$  and Jiwoong Park  $^{*,\ddagger,\$,\parallel}$ 

Supporting Information

ABSTRACT: Quantum computing based on superconducting qubits requires the understanding and control of the materials, device architecture, and operation. However, the materials for the central circuit element, the Josephson junction, have mostly been focused on using the AlO<sub>x</sub> tunnel barrier. Here, we demonstrate Josephson junctions and superconducting qubits employing two-dimensional materials as the tunnel barrier. We batch-fabricate and design the critical Josephson current of these devices via layer-by-layer stacking N layers of MoS<sub>2</sub> on the large scale. Based on such junctions, MoS<sub>2</sub> transmon qubits are engineered and



characterized in a bulk superconducting microwave resonator for the first time. Our work allows Josephson junctions to access the diverse material properties of two-dimensional materials that include a wide range of electrical and magnetic properties, which can be used to study the effects of different material properties in superconducting qubits and to engineer novel quantum circuit elements in the future.

KEYWORDS: two-dimensional materials, molybdenum disulfide, tunnel barrier, Josephson junctions, superconducting qubits

Recent developments in the device architecture and operation of the state-of-the-art superconducting qubits have allowed the technology to initiate practical applications in quantum computing. 1-5 At the center of such qubit is the Josephson junction, which is composed of two superconductors (SCs) separated by an ultrathin tunnel barrier (Figure 1). Currently, the tunnel barrier for Josephson junctions is mostly fabricated using AlO, that is natively grown on Al, as the existing fabrication method for such structure provides high quality junctions for superconducting qubits to achieve excellent coherence time. However, AlO<sub>x</sub> has been reported to have thickness inhomogeneity<sup>6</sup> and defects that may compromise the qubit performance.<sup>7-9</sup> Moreover, new materials with different properties for fabricating Josephson junctions are expected to introduce novel functionalities and circuit elements for superconducting qubits. As such, intensive efforts to implement new materials in Josephson junctions have emerged recently. This includes directly replacing the tunnel barrier such as the Re/epitaxial sapphire/Al and NbN/AlN/NbN vertical junctions, 10,11 as well as utilizing a lateral Josephson junction geometry to implement nanowires/nanotubes, 12-14 two-dimensional (2D)

electron gas, 15 and graphene 16 as the weak link for new functionalities such as voltage-tunable qubits.

Two-dimensional materials could provide excellent solidstate systems for generating novel tunnel barriers for Josephson junctions with their wide varieties of electrical and magnetic properties. 17-19 The atomic thinness of monolayer 2D materials (~a few Å) allows them to be used as tunnel barriers. Their van der Waals layered structures further enable the precise design of the barrier thickness through layer-bylayer stacking, whereby each layer can be a different 2D material to generate a heterostructure barrier. In addition, they can be released from the substrate as a freestanding atomically thin film, making it possible to combine 2D materials with different SCs. These unique properties would allow for the design of the tunnel barrier band structure using 2D materials with different band gaps and band offsets,20 the study of Josephson junction in the ultimately short regime, 21 and the

Received: September 19, 2019 Revised: October 23, 2019 Published: October 29, 2019

Downloaded via CORNELL UNIV on November 15, 2019 at 21:08:05 (UTC). See https://pubs.acs.org/sharingguidelines for options on how to legitimately share published articles.

<sup>&</sup>lt;sup>†</sup>School of Applied and Engineering Physics, Cornell University, Ithaca, New York 14853, United States

<sup>&</sup>lt;sup>‡</sup>Pritzker School of Molecular Engineering, University of Chicago, Chicago, Illinois 60637, United States

<sup>§</sup>James Franck Institute, University of Chicago, Chicago, Illinois 60637, United States

Department of Physics, University of Chicago, Chicago, Illinois 60637, United States

Department of Chemistry, University of Chicago, Chicago, Illinois 60637, United States

 $<sup>^\</sup>perp$ Department of Chemistry and Chemical Biology, Cornell University, Ithaca, New York 14853, United States

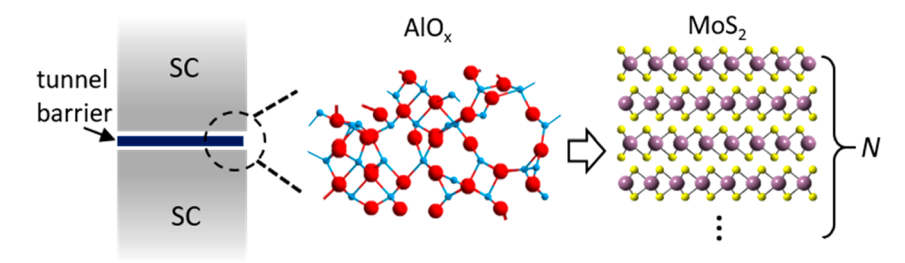


Figure 1. Schematics of the structure of a Josephson junction, wherein an ultrathin tunnel barrier is sandwiched between two superconductors (SCs). The barrier is mostly made of amorphous aluminum oxide natively grown on aluminum. In this work, we replace the barrier material with N-layer  $MoS_2$ , where the number of layers N can be designed via layer-by-layer stacking.

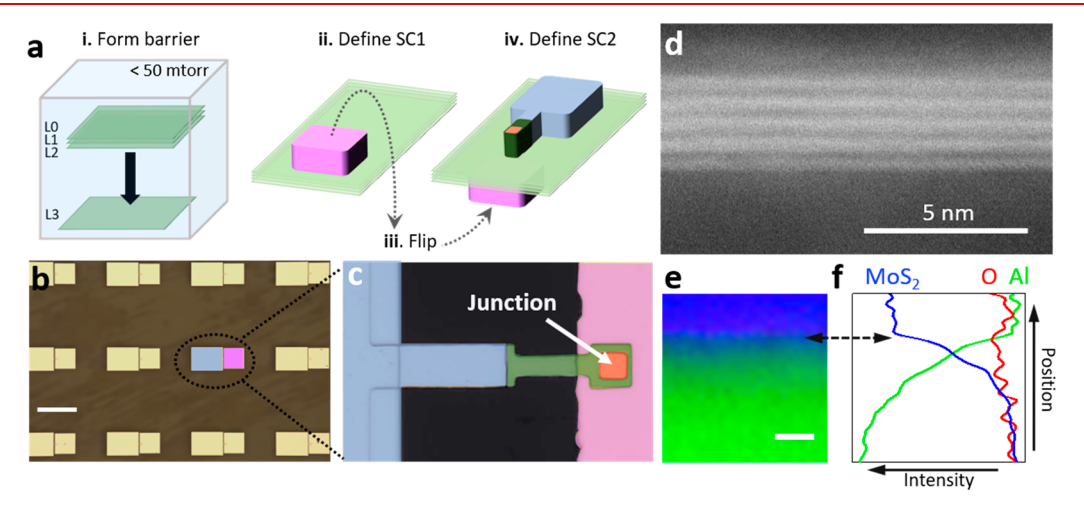


Figure 2. Barrier-first method. (a) Fabrication steps for the barrier-first method. See main text for a detailed description. (b) An optical image of a batch-fabricated Al/4L-MoS<sub>2</sub>/Al Josephson junction array. The circled device is false-colored, where the purple is the bottom electrode or SC1, and the blue is the top electrode or SC2. The scale bar is 0.4 mm. (c) Zoom-in image of an Al/4L-MoS<sub>2</sub>/Al Josephson junction. Blue, top electrode pad; green, suspended aluminum airbridge; red, the Al/MoS<sub>2</sub>/Al junction; purple, bottom electrode. Junction size is 5 by 5  $\mu$ m<sup>2</sup>. (d) Cross-sectional HAADF STEM image of an Al/5L-MoS<sub>2</sub>/Al junction. The five bright lines in the middle are the vacuum-stacked MoS<sub>2</sub>. (e) Elemental mapping across the bottom interface of the junction. Green, Al (from EELS); red, O (from EELS); blue, MoS<sub>2</sub> (from ADF intensity). The scale bar is 2 nm. The arrow marks the Al/MoS<sub>2</sub> interface. (f) Signal intensity versus location corresponding to (e). Colors for each element are the same as in (e).

fabrication of novel quantum circuit components such as  $\pi$ junctions using 2D magnets. 22-24 Nevertheless, as most of the common SCs are easily oxidized, it is essential to have a method that can maintain oxide-free interfaces between the SCs and the 2D material barrier while keeping the advantages of the above designability and being scalable to a technologically relevant scale. In this Letter, we demonstrate the Josephson junctions with a 2D material barrier using Al/ MoS<sub>2</sub>/Al tunnel junctions as an example (Figure 1, right). We first present our process, named as barrier-first method, that provides a scalable fabrication solution for integrating 2D materials with oxygen-sensitive bulk SCs. The Josephson effect in these MoS<sub>2</sub>-based tunnel junctions are then demonstrated, where the critical current can be tuned over orders of magnitude through layer-by-layer stacking of MoS2 monolayers. Finally, we demonstrate the engineering and operation of superconducting qubits with a MoS2 tunnel barrier for the first time.

The concept of our barrier-first method is described in Figure 2a. We start with large-scale monolayers of  $MoS_2$  that are grown by metal—organic chemical vapor deposition (MOCVD) on  $SiO_2/Si$  substrates, and stack them layer-by-layer in a vacuum chamber (<50 mTorr) until we reach the targeted number of layers N for the designed thickness of the tunnel barrier (step i). The details of the large-scale growth

and vacuum stacking have been reported in our previous work. 20,25 In step ii, we define the first superconducting electrodes (SC1) by directly evaporating Al metal onto the stacked MoS<sub>2</sub> using a shadow mask. In step iii, the Al-on-MoS<sub>2</sub> thin film is released from the substrate, flipped over, and transferred onto the final substrate (sapphire). The SC1 now becomes the bottom electrode, where the MoS<sub>2</sub> side is exposed on top. The MoS<sub>2</sub> film here provides the needed encapsulation of the bottom aluminum from the air and various chemicals in the following process besides serving as the tunnel barrier. In step iv, we directly evaporate aluminum onto the MoS<sub>2</sub> again and define the second electrodes (SC2) using standard photolithography and reactive-ion etching. An airbridge is fabricated to gain access to the junction without using a dielectric as a spacer to separate the top electrodes from the bottom electrodes in order to reduce microwave loss during qubit measurement. (See Supporting Information (SI) for details of the electrode fabrication and Figure S3 for the SEM image of the airbridge.)

As illustrated, we start with making the tunnel barrier instead of growing it on top of the bottom electrodes as commonly done. This reversed process sequence provides us with three key advantages. First, it allows us to design the barrier structure independently of the electrodes. Second, by directly depositing SC electrodes on either side, oxide contamination at the

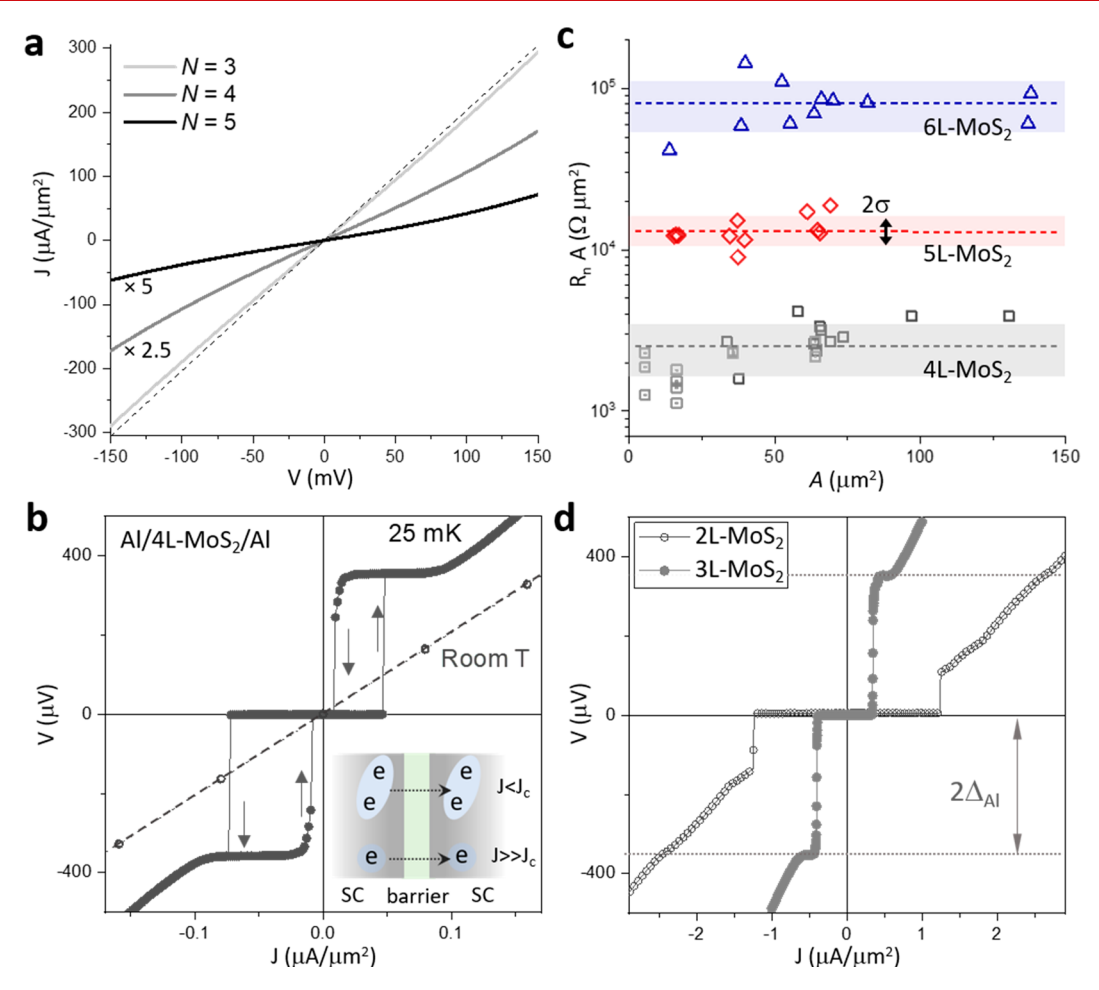


**Figure 3.** Electrical characterization and Josephson effect. (a) Room temperature J-V curves of junctions with different N, where N=3, 4, and 5. The values of the current density is multiplied by 1, 2.5, and 5, respectively, for clarity. The dashed line is a straight line for reference. (b) J-V curves of an Al/4L-MoS<sub>2</sub>/Al tunnel junction at room temperature (empty dots) and 25 mK (solid). The arrows indicate the current sweeping directions, starting from zero to positive bias. Inset: Schematics of the Josephson effect and normal tunneling at different current biases. (c) Resistance—area product ( $R_nA$ ) versus junction area (A) of MoS<sub>2</sub> junctions with N=4, 5, and 6.  $\sigma$  is the standard deviation, and the color bands denote 2 $\sigma$  of each N. Note that the 4L-MoS<sub>2</sub> data set includes two batches of devices, which are shown with different symbols, squares and squares with dots.  $\sigma$  for the 4L-MoS<sub>2</sub> devices includes both batches. (d) Josephson curves of Al/NL-MoS<sub>2</sub>/Al with N=2 and 3, both curves are measured from positive to negative current bias.  $\Delta_{Al}$  is the superconducting gap of Al.

barrier/electrode interfaces are avoided, as shown in Figure 2d–f. Third, as the  $MoS_2$  tunnel barrier is generated by stacking wafer-scale  $MoS_2$  monolayers layer-by-layer, the barrier thickness is precisely controlled on the large scale and the devices can be batch fabricated as arrays. An optical microscope image of the as-fabricated junction array is presented in Figure 2b. The detailed structure of the Al/ $MoS_2/Al$  tunnel device is shown in the false-colored zoom-in image in Figure 2c, which includes the top (blue) and bottom (purple) electrode, an airbridge (green), and the tunnel junction (red, 5 by 5  $\mu$ m $^2$ ).

Figure 2d—f confirms that the barrier-first method maintains oxide free interfaces between the MoS<sub>2</sub> and Al, as the MoS<sub>2</sub> barrier film protects the bottom Al throughout the fabrication process until the evaporation of top Al (i.e., in steps iii and iv). Figure 2d first shows a cross-sectional high-angle annular dark-field (HAADF) STEM image of an Al/5L-MoS<sub>2</sub>/Al junction. (See also SI for remarks on sample preparation.) The 5L-MoS<sub>2</sub> appears in the image as the five bright lines in the middle, where the monolayer thickness is roughly 0.64 nm. As shown, all MoS<sub>2</sub> layers are parallel to each other without defects and show clean interlayer interfaces, demonstrating the quality of

our vacuum-stacked MoS<sub>2</sub> barrier. The chemical compositions across the bottom interface between MoS<sub>2</sub> and aluminum are further characterized using electron energy loss spectroscopy (EELS). Figure 2e shows the elemental map with colors representing Al (green, from EELS), O (red, from EELS), and MoS<sub>2</sub> (blue, from ADF intensity), and Figure 2f presents the corresponding signal intensity from each element along the vertical axis. It is observed that the Al (Mo) signal intensity roughly reaches minimum (maximum) around the Al/MoS<sub>2</sub> interface, and the O signal remains close to the noise level everywhere across the interface. This evidence supports that there is no oxide contamination at the interface between MoS<sub>2</sub> and Al, confirming that we have successfully maintained intrinsic interfaces in our Al/MoS<sub>2</sub>/Al junctions.

We now discuss the electrical properties and DC Josephson effect of the as-fabricated  $Al/MoS_2/Al$  junctions. At room temperature, all  $Al/NL-MoS_2/Al$  junctions (N=3,4,5) exhibit the characteristic nonlinear J-V curves of normal tunneling as shown in Figure 3a. The current decreases exponentially ( $\sim$ a factor of 5) with each additional layer in the barrier, which again agrees with the exponential dependence of tunnel current on the thickness of the barrier. We further

characterize the low-temperature properties of the junctions in a dilution fridge at 25 mK and observe a dramatic transition of the J-V curve in the zero-bias regime as displayed in Figure 3b, which is measured from a representative 4L-MoS $_2$  device. Four distinct features are clearly shown in stark contrast to that at room temperature in this low bias regime: (1) there is a finite current up to a critical current density  $J_c$  at V=0, (2) an abrupt switch from zero voltage to roughly  $\pm 350~\mu V$  after  $J_c$ , (3) behavior similar to that at room temperature as the current bias is further increased, and (4) the J-V curves show hysteresis depending on the current sweeping directions.

The first three features are characteristic of the Josephson effect across a tunnel barrier as illustrated in the inset schematics of Figure 3b. Below  $J_c$ , the Cooper pair can directly tunnel through the barrier without energy dissipation, and thus, no finite voltage is measured (i.e., the DC Josephson effect). Once the current bias exceeds  $J_{c}$  excess current can only be carried by generating quasiparticles for tunneling. This requires a voltage that is twice the size of the superconducting gap  $(2\Delta)$ , which is the voltage the device reaches after  $J_c$ . We can accordingly estimate  $2\Delta$  of our aluminum to be 350  $\mu$ V, consistent with the reported value for bulk Al.<sup>26</sup> At a voltage much larger than  $2\Delta$ , normal single particle tunneling that happens at room temperature dominates current transport again. The hysteresis, however, results from the underdamped nature of our junction circuits.<sup>27</sup> The results presented above directly demonstrate that we have successfully fabricated Josephson junctions with the Al/MoS<sub>2</sub>/Al vertical structure.

Precise control of the tunnel resistance and Josephson current is essential to engineer superconducting qubits with proper quantum states for operation. This can be realized with a large tuning range and high fidelity through controlling the layer number N of MoS2. Figure 3c presents the zero-bias tunnel resistance-area product  $(R_nA)$  of different N and junction area A. For devices with the same N, R<sub>n</sub>A remains approximately constant as expected for tunnel junctions (dashed lines). For devices with the same A,  $R_nA$  can be tuned by orders of magnitude by varying N. As shown by the Al/5L-MoS<sub>2</sub>/Al junction array, which is batch-fabricated over a 5 by 5 mm<sup>2</sup> area on a single chip, we can achieve good homogeneity with a standard deviation  $\sigma$  that is 17% of the average tunnel resistance of the array. This spread is significantly smaller compared to the factor of 5 change when adding or reducing one layer of MoS<sub>2</sub> in the barrier. As the critical current  $I_c$  of a Josephson junction is proportional to  $\Delta/R_{\rm n}$ , the  $I_{\rm c}$  also depends on N exponentially. This is demonstrated in Figure 3d, where we show that the  $J_c$  of the 2L-MoS<sub>2</sub> tunnel barrier is  $\sim$ 1.2  $\mu$ A/ $\mu$ m<sup>2</sup>, 3L-MoS<sub>2</sub> is  $\sim$ 0.36  $\mu A/\mu m^2$ , and 4L-MoS<sub>2</sub> is ~0.04  $\mu A/\mu m^2$  (from Figure 3b). Accordingly, one can design the  $I_c$  of a junction with N and A as the two independent variables, i.e.,  $I_c(N, A) = J_c(N)A$ , which scales exponentially with N but linearly with A. This layer-bylayer tunability for designing the I<sub>c</sub> makes the MoS<sub>2</sub> barrier a useful material system for engineering superconducting qubits as shown in Figure 4.

We briefly note here that we observe a crossover of our Al/NL-MoS $_2$ /Al junctions from a superconductor—insulator—superconductor (SIS) junction for  $N \geq 3$  to a superconductor—normal metal—superconductor (SNS) junction for N=2. This can be seen by the switching after  $I_c$  as the voltage immediately reaches  $V=\pm 2\Delta_{\rm Al}$  for  $N\geq 3$ , while it reaches sub-gap values for N=2. Figure S5 further shows multiple Andreev reflection peaks for N=2, which are absent

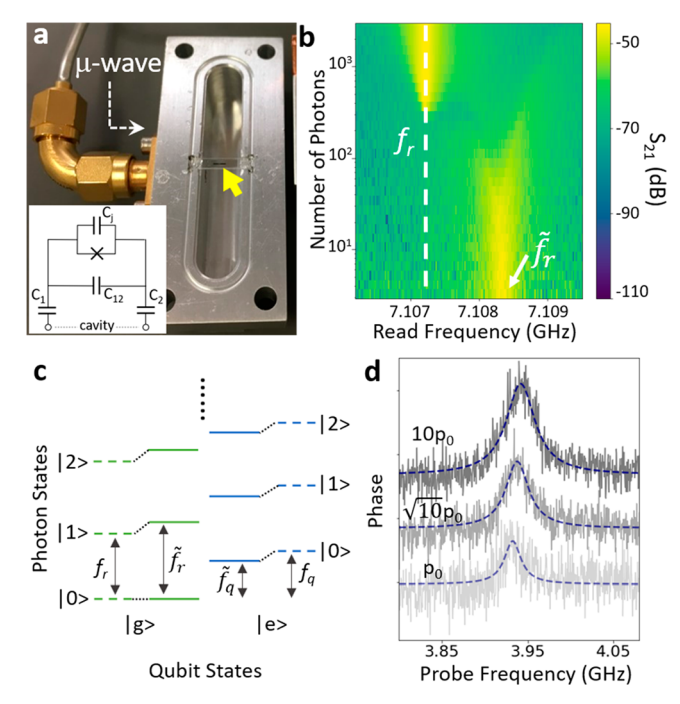


Figure 4. Superconducting qubit with a MoS<sub>2</sub> tunnel barrier. (a) The measurement setup. Microwave tones are input using a coaxial cable to the aluminum resonator as indicated, while the signal is collected from a second cable on the lid (not shown). The yellow arrow indicates the Al/4L-MoS<sub>2</sub>/Al Josephson junction and the capacitor pads. Inset: An effective circuit diagram for the setup.  $C_1$  and  $C_2$  are the capacitance of the pads, and  $C_{12}$  is the interpad capacitance. (b) The response of the qubit-resonator system as a function of the applied microwave power. The lower frequency peak corresponds to the cavity frequency  $f_r$  without hybridization with the qubit, while the higher frequency peak  $\tilde{f}_r$  corresponds to the resonance with hybridization. (c) Schematic of the quantum states that contribute to the response in (b).  $|i\rangle$  with i = 0, 1, 2 are the photon number states of the resonator, while |g\>, |e\> denote the ground and first excited states of the qubit. The dashed (solid) lines denote the bare (dressed) states of the system before (after) hybridization. (d) Qubit excitation at different excitation powers, where  $p_0$  is the probe power at the sample and is  $\sim 8 \times 10^{-10}$  mW. Dashed lines are fits to the Lorentzian peaks.

for  $N \ge 3$ . Such crossover depending on N may be due to the semiconducting nature of our tunnel barrier. MoS<sub>2</sub> has a much smaller band gap ( $\sim 1.9$  eV for monolayer and lower for multilayers) than other common barriers such as  $AlO_x$  (4–9 eV<sup>28</sup>), which makes the band profile of the junction more sensitive to the geometry. The details of the crossover, however, are beyond the scope of this work and thus will be studied in the future.

With  $I_c$  being a function of (N, A), we can now design the parameters for the  $Al/MoS_2/Al$  superconducting qubits accordingly. For instance, in a transmon qubit, the transition energy from the ground state  $|g\rangle$  to the first excited state  $|e\rangle$  is  $E = \sqrt{8E_JE_c} - E_c$ , where  $E_J = \hbar I_c/2e_0$  is the Josephson energy,  $e_0$  is the electron charge, and  $E_c = e_0^2/2C$  is the capacitive energy of the overall circuit shown in the circuit diagram of Figure 4a (inset). Designing E, therefore, can be achieved by choosing (N, A) for  $E_J$  and adjusting  $E_c$  using the overall circuit capacitance in addition to the Josephson junction capacitance. In Figure 4, we fabricate a single  $Al/AL-MoS_2/Al$  Josephson junction with a junction area of 2 by 2  $\mu$ m<sup>2</sup> on a sapphire substrate, which gives us a transition frequency  $f_q = E/h = 3.94$ 

GHz between the lowest energy states. As indicated by the yellow arrow in Figure 4a, the junction is placed at the center of an aluminum microwave bulk cavity resonator designed to have a resonance frequency at  $f_{\rm r}=7.107$  GHz as determined by the dimensions of the cavity. The coupling strength g between the MoS<sub>2</sub> qubit and the resonator is determined by the geometry of the electrodes of the MoS<sub>2</sub> qubit, which is designed to be  $\sim\!60$  MHz in our experiment based on black box quantization. As  $g\ll f_{\rm r}-f_{\rm q}$ , the qubit and the resonator are coupled in the dispersive regime.

To confirm the coupling between the qubit and the resonator, we first measure the response of the system by sweeping the microwave frequency around  $f_r$  while increasing the photon number in the cavity by varying the applied microwave power as shown in Figure 4b. For small photon number ( $\ll$ 100), we see a single peak at around 7.108 GHz (denoted as  $f_r$ ). In the intermediate regime, the response splits into two peaks, of which the splitting increases and intensity decreases as the photon number further increased. Eventually at large photon number, the peak jumps to  $f_r$ . The above power dependence is characteristic of the hybridization arising from the Jaynes-Cummings interaction between a resonator and a qubit.<sup>33</sup> Figure 4c illustrates the quantum states of the qubit-resonator system, and the dashed (solid) lines denote the bare (dressed) states of the system before (after) their hybridization. Near the single photon power at the device,  $f_r$ corresponds to the excitation from the ground to the lowest excited state of the qubit-resonator hybrid system, i.e.,  $(|g\rangle|1\rangle + \frac{g}{f_r - f_a}|e\rangle|0\rangle$ ). As the photon number increases, the

system enters a region of semiclassical bistability that presumably contributes to the observed power dependence as previously reported.<sup>33</sup> Above the critical photon number, the system frequency is no longer dressed by the qubit–resonator interaction and becomes insensitive to the qubit state. The experiment above indicates successful coupling of the MoS<sub>2</sub> qubit to the bulk microwave resonator, with behavior that is well understood with existing theory. This allows us to operate and readout the MoS<sub>2</sub> transmon with established techniques in superconducting circuit quantum electrodynamics (QED).

In Figure 4d, we further demonstrate the manipulation of the  $MoS_2$  qubit by using a microwave drive tone at the qubit dressed state frequency  $\tilde{f}_{q'}$  to alter the qubit states while reading the state of the qubit with a readout microwave tone at  $\tilde{f}_r$  in the low photon number region. We measure the phase shift of the readout tone as the drive tone is swept around  $\tilde{f}_{q'}$ . Indeed, the qubit transition is observed as a large phase shift when the microwave sweeps through  $\tilde{f}_{q'}$  showing that we have put the qubit into the excited state. As the excitation power is increased, the peak is significantly broadened as a result of the stimulated relaxation of the qubit due to the applied  $\tilde{f}_q$  microwave tone ( $p_0 \approx 8 \times 10^{-10}$  mW). We measure the power dependence of the peak and extrapolate for the peak width at zero-power. This gives us an estimate of the coherence time  $T_2^*$ , which is  $\sim 12$  ns for the device measured (Figure S6).

Here, we propose three sources that may have contributed to the relatively short coherence time of our  $MoS_2$  qubits as well as potential solutions to address them to improve the coherent time. The first source is the device geometry. As an example, our large junction size (2 by 2  $\mu$ m<sup>2</sup>) based on the photolithography process is 2 orders of magnitude larger than

those of typical AlO<sub>x</sub> transmon qubits  $((\sim \text{hundreds})^2 \text{ nm})$ . In previous reports on AlO<sub>x</sub> phase qubits, the energy relaxation time  $(T_1)$  in larger AlO<sub>x</sub> junctions (>70  $\mu$ m<sup>2</sup>) was 10–20 ns, mainly limited by the number of two-level systems in the barrier. It is shown to improve by reducing the junction size until other decoherence sources dominate. 34,35 For our qubits, shrinking the junction area may have the same positive effect, while the reduced  $E_{\rm I}$  due to the smaller junction area can be compensated by adjusting the N of the barrier or switching to another 2D material that forms a lower tunnel barrier height. The second possible source is the unoptimized fabrication process. For example, the use of photoresist to define the contact between top aluminum and the MoS2 tunnel barrier would leave polymer residues that degrade the junction quality.<sup>36</sup> Such residue may be reduced by, for instance, Ar/ H<sub>2</sub> annealing of the top interface before evaporation.<sup>37</sup> Lastly, the dielectric loss of the MOCVD-grown MoS<sub>2</sub> may contribute to decoherence, such as due to the presence of defects. Currently, the defect characteristics and the microwave properties of 2D materials are not well-understood in the low temperature (25 mK) and low power (near single photon) regimes where qubits operate, in part hindered by the underdeveloped fabrication method for suitable devices.<sup>38</sup> Our work, hence, may provide a viable way to study such properties of 2D materials in this previously inaccessible regime.

In conclusion, we have fabricated Josephson junctions and superconducting qubits made with MoS2 tunnel barriers using our barrier-first method. The junction and qubit properties can be precisely tuned layer-by-layer by exploiting the van der Waals layered structure of MoS<sub>2</sub> to design the barrier thickness. Our method opens up the possibility of making designable Josephson junctions with a MoS<sub>2</sub> tunnel barrier and can potentially be applied to other similar 2D materials such as WSe<sub>2</sub> and hBN, each having a distinct band gap, band offset, and other physical properties. In the future, this may be generalized to other combinations of superconductors and 2D materials including 2D magnets for fabricating  $\pi$ -Josephson junctions. Our method here will provide a powerful platform to study the effects of different material properties in superconducting qubit circuits under different geometries, and to explore new device structures that could lead to novel quantum circuit components for quantum computing.

#### ASSOCIATED CONTENT

#### S Supporting Information

The Supporting Information is available free of charge on the ACS Publications website at DOI: 10.1021/acs.nanolett.9b03886.

Detailed description of the barrier-first method;  $^{39,40}$  methods for cross-sectional STEM; setup for DC and microwave measurement in dilution fridge; SEM image of the airbridge; remarks on sample preparation for cross-sectional STEM; SNS to SIS crossover between 2L- and 3L-MoS<sub>2</sub> Josephson junctions; remarks on the resistance of Al/MoS<sub>2</sub>/Al junctions; estimating  $T_2^*$  of MoS<sub>2</sub> qubits (PDF)

# AUTHOR INFORMATION

## **Corresponding Authors**

\*E-mail: david.schuster@uchicago.edu.

\*E-mail: jwpark@uchicago.edu.

## ORCID

Kan-Heng Lee: 0000-0001-9557-5592

Notes

The authors declare no competing financial interest.

#### ACKNOWLEDGMENTS

We thank Gerwin Koolstra, Hung-Shen Chang, Peter Duda, and Youpeng Zhong for helpful scientific discussions. This work was primarily supported by the University of Chicago Materials Research Science and Engineering Center (NSF DMR-1420709) and the Cornell Center for Materials Research (NSF DMR-1719875), both of which are funded by the National Science Foundation. Additional funding was provided by the Air Force Office of Scientific Research (FA9550-16-1-0031 and FA9550-18-1-0480) and the Samsung Advanced Institute of Technology. The Titan microscope was acquired with the NSF MRI grant DMR-1429155. K.-H.L. acknowledges support by the Ministry of Education of Taiwan through the Government Scholarship to Study Abroad. F.M. acknowledges support by the National Science Foundation Graduate Research Fellowship Program under Grant No. DGE-1746045. Y.Z. acknowledges support by the Camille and Henry Dreyfus Foundation, Inc., under the Dreyfus Environmental Postdoc award EP-16-094.

## REFERENCES

- (1) Wallraff, A.; Schuster, D. I.; Blais, A.; Frunzio, L.; Huang, R.-S.; Majer, J.; Kumar, S.; Girvin, S. M.; Schoelkopf, R. J. Strong Coupling of a Single Photon to a Superconducting Qubit Using Circuit Quantum Electrodynamics. *Nature* **2004**, *431* (7005), 162–167.
- (2) Koch, J.; Yu, T. M.; Gambetta, J.; Houck, A. A.; Schuster, D. I.; Majer, J.; Blais, A.; Devoret, M. H.; Girvin, S. M.; Schoelkopf, R. J. Charge-Insensitive Qubit Design Derived from the Cooper Pair Box. *Phys. Rev. A: At., Mol., Opt. Phys.* **2007**, *76* (4), 042319.
- (3) Buluta, I.; Nori, F. Quantum Simulators. Science 2009, 326 (5949), 108-111.
- (4) Devoret, M. H.; Schoelkopf, R. J. Superconducting Circuits for Quantum Information: An Outlook. *Science* **2013**, 339 (6124), 1169–1174
- (5) Neill, C.; Roushan, P.; Kechedzhi, K.; Boixo, S.; Isakov, S. V.; Smelyanskiy, V.; Megrant, A.; Chiaro, B.; Dunsworth, A.; Arya, K.; Barends, R.; Burkett, B.; Chen, Y.; Chen, Z.; Fowler, A.; Foxen, B.; Giustina, M.; Graff, R.; Jeffrey, E.; Huang, T.; Kelly, L.; Klimov, P.; Lucero, E.; Mutus, J.; Neeley, M.; Quintana, C.; Sank, D.; Vainsencher, A.; Wenner, J.; White, T. C.; Neven, H.; Martinis, J. M. A Blueprint for Demonstrating Quantum Supremacy with Superconducting Qubits. *Science* 2018, 360 (6385), 195–199.
- (6) Zeng, L. J.; Nik, S.; Greibe, T.; Krantz, P.; Wilson, C. M.; Delsing, P.; Olsson, E. Direct Observation of the Thickness Distribution of Ultrathin AlO<sub>x</sub> Barriers in Al/AlO<sub>x</sub>/Al Josephson Junctions. *J. Phys. D: Appl. Phys.* **2015**, *48* (39), 395308.
- (7) Oliver, W. D.; Welander, P. B. Materials in Superconducting Quantum Bits. MRS Bull. 2013, 38 (10), 816–825.
- (8) McDermott, R. Materials Origins of Decoherence in Superconducting Qubits. *IEEE Trans. Appl. Supercond.* **2009**, *19* (1), 2–13. (9) Klimov, P. V.; Kelly, J.; Chen, Z.; Neeley, M.; Megrant, A.; Burkett, B.; Barends, R.; Arya, K.; Chiaro, B.; Chen, Y.; Dunsworth, A.; Fowler, A.; Foxen, B.; Gidney, C.; Giustina, M.; Graff, R.; Huang, T.; Jeffrey, E.; Lucero, E.; Mutus, J. Y.; Naaman, O.; Neill, C.; Quintana, C.; Roushan, P.; Sank, D.; Vainsencher, A.; Wenner, J.; White, T. C.; Boixo, S.; Babbush, R.; Smelyanskiy, V. N.; Neven, H.; Martinis, J. M. Fluctuations of Energy-Relaxation Times in Superconducting Qubits. *Phys. Rev. Lett.* **2018**, *121* (9), 090502.
- (10) Oh, S.; Cicak, K.; Kline, J. S.; Sillanpaa, M. A.; Osborn, K. D.; Whittaker, J. D.; Simmonds, R. W.; Pappas, D. P. Elimination of Two Level Fluctuators in Superconducting Quantum Bits by an Epitaxial

Tunnel Barrier. Phys. Rev. B: Condens. Matter Mater. Phys. 2006, 74 (10), 100502.

- (11) Nakamura, Y.; Terai, H.; Inomata, K.; Yamamoto, T.; Qiu, W.; Wang, Z. Superconducting Qubits Consisting of Epitaxially Grown NbN/AlN/NbN Josephson Junctions. *Appl. Phys. Lett.* **2011**, 99 (21), 212502.
- (12) Larsen, T. W.; Petersson, K. D.; Kuemmeth, F.; Jespersen, T. S.; Krogstrup, P.; Nygård, J.; Marcus, C. M. Semiconductor-Nanowire-Based Superconducting Qubit. *Phys. Rev. Lett.* **2015**, *115* (12), 127001.
- (13) de Lange, G.; van Heck, B.; Bruno, A.; van Woerkom, D. J.; Geresdi, A.; Plissard, S. R.; Bakkers, E. P. A. M.; Akhmerov, A. R.; DiCarlo, L. Realization of Microwave Quantum Circuits Using Hybrid Superconducting-Semiconducting Nanowire Josephson Elements. *Phys. Rev. Lett.* **2015**, *115* (12), 127002.
- (14) Mergenthaler, M.; Nersisyan, A.; Patterson, A.; Esposito, M.; Baumgartner, A.; Schönenberger, C.; Briggs, G. A. D.; Laird, E. A.; Leek, P. J. Realization of a Carbon-Nanotube-Based Superconducting Qubit. *ArXiv*190410132 *Cond-Mat Physicsquant-Ph*, **2019**.
- (15) Casparis, L.; Connolly, M. R.; Kjaergaard, M.; Pearson, N. J.; Kringhøj, A.; Larsen, T. W.; Kuemmeth, F.; Wang, T.; Thomas, C.; Gronin, S.; Gardner, G. C.; Manfra, M. J.; Marcus, C. M.; Petersson, K. D. Superconducting Gatemon Qubit Based on a Proximitized Two-Dimensional Electron Gas. *Nat. Nanotechnol.* **2018**, *13* (10), 915–919.
- (16) Wang, J. I.-J.; Rodan-Legrain, D.; Bretheau, L.; Campbell, D. L.; Kannan, B.; Kim, D.; Kjaergaard, M.; Krantz, P.; Samach, G. O.; Yan, F.; Yoder, J. L.; Watanabe, K.; Taniguchi, T.; Orlando, T. P.; Gustavsson, S.; Jarillo-Herrero, P.; Oliver, W. D. Coherent Control of a Hybrid Superconducting Circuit Made with Graphene-Based van Der Waals Heterostructures. *Nat. Nanotechnol.* **2019**, *14*, 120.
- (17) Novoselov, K. S.; Jiang, D.; Schedin, F.; Booth, T. J.; Khotkevich, V. V.; Morozov, S. V.; Geim, A. K. Two-Dimensional Atomic Crystals. *Proc. Natl. Acad. Sci. U. S. A.* **2005**, *102* (30), 10451–10453.
- (18) Geim, A. K.; Grigorieva, I. V. Van Der Waals Heterostructures. *Nature* **2013**, 499 (7459), 419–425.
- (19) Novoselov, K. S.; Mishchenko, A.; Carvalho, A.; Neto, A. H. C. 2D Materials and van Der Waals Heterostructures. *Science* **2016**, 353 (6298), No. aac9439.
- (20) Kang, K.; Lee, K.-H.; Han, Y.; Gao, H.; Xie, S.; Muller, D. A.; Park, J. Layer-by-Layer Assembly of Two-Dimensional Materials into Wafer-Scale Heterostructures. *Nature* **2017**, *550* (7675), 229–233.
- (21) Lee, G.-H.; Kim, S.; Jhi, S.-H.; Lee, H.-J. Ultimately Short Ballistic Vertical Graphene Josephson Junctions. *Nat. Commun.* **2015**, *6*, 6181.
- (22) Huang, B.; Clark, G.; Navarro-Moratalla, E.; Klein, D. R.; Cheng, R.; Seyler, K. L.; Zhong, D.; Schmidgall, E.; McGuire, M. A.; Cobden, D. H.; Yao, W.; Xiao, D.; Jarillo-Herrero, P.; Xu, X. Layer-Dependent Ferromagnetism in a van Der Waals Crystal down to the Monolayer Limit. *Nature* **2017**, *546* (7657), 270–273.
- (23) Ryazanov, V. V.; Oboznov, V. A.; Rusanov, A. Y.; Veretennikov, A. V.; Golubov, A. A.; Aarts, J. Coupling of Two Superconductors through a Ferromagnet: Evidence for a  $\pi$  Junction. *Phys. Rev. Lett.* **2001**, 86 (11), 2427–2430.
- (24) Vávra, O.; Gaži, S.; Golubović, D. S.; Vávra, I.; Dérer, J.; Verbeeck, J.; Van Tendeloo, G.; Moshchalkov, V. V. 0 and r Phase Josephson Coupling through an Insulating Barrier with Magnetic Impurities. *Phys. Rev. B: Condens. Matter Mater. Phys.* **2006**, 74 (2), 020502.
- (25) Kang, K.; Xie, S.; Huang, L.; Han, Y.; Huang, P. Y.; Mak, K. F.; Kim, C.-J.; Muller, D.; Park, J. High-Mobility Three-Atom-Thick Semiconducting Films with Wafer-Scale Homogeneity. *Nature* **2015**, 520 (7549), 656–660.
- (26) Kittel, C. Introduction to Solid State Physics, 8th ed.; Wiley, 2005.
- (27) Martinis, J. M.; Kautz, R. L. Classical Phase Diffusion in Small Hysteretic Josephson Junctions. *Phys. Rev. Lett.* **1989**, *63* (14), 1507–1510.

(28) Canulescu, S.; Rechendorff, K.; Borca, C. N.; Jones, N. C.; Bordo, K.; Schou, J.; Pleth Nielsen, L.; Hoffmann, S. V.; Ambat, R. Band Gap Structure Modification of Amorphous Anodic Al Oxide Film by Ti-Alloying. *Appl. Phys. Lett.* **2014**, *104* (12), 121910.

- (29) Kleinsasser, A. W.; Jackson, T. N.; McInturff, D.; Rammo, F.; Pettit, G. D.; Woodall, J. M. Crossover from Tunneling to Metallic Behavior in Superconductor-semiconductor Contacts. *Appl. Phys. Lett.* **1990**, *57* (17), 1811–1813.
- (30) Island, J. O.; Steele, G. A.; Zant, H. S. J. van der; Castellanos-Gomez, A. Thickness Dependent Interlayer Transport in Vertical MoS <sub>2</sub> Josephson Junctions. 2D Mater. **2016**, 3 (3), 031002.
- (31) Liu, Y.; Guo, J.; Zhu, E.; Liao, L.; Lee, S.-J.; Ding, M.; Shakir, I.; Gambin, V.; Huang, Y.; Duan, X. Approaching the Schottky-Mott Limit in van Der Waals Metal-Semiconductor Junctions. *Nature* **2018**, 557 (7707), 696.
- (32) Nigg, S. E.; Paik, H.; Vlastakis, B.; Kirchmair, G.; Shankar, S.; Frunzio, L.; Devoret, M. H.; Schoelkopf, R. J.; Girvin, S. M. Black-Box Superconducting Circuit Quantization. *Phys. Rev. Lett.* **2012**, *108* (24), 240502.
- (33) Bishop, L. S.; Ginossar, E.; Girvin, S. M. Response of the Strongly Driven Jaynes-Cummings Oscillator. *Phys. Rev. Lett.* **2010**, 105 (10), 100505.
- (34) Cooper, K. B.; Steffen, M.; McDermott, R.; Simmonds, R. W.; Oh, S.; Hite, D. A.; Pappas, D. P.; Martinis, J. M. Observation of Quantum Oscillations between a Josephson Phase Qubit and a Microscopic Resonator Using Fast Readout. *Phys. Rev. Lett.* **2004**, 93 (18), 180401.
- (35) Martinis, J. M.; Cooper, K. B.; McDermott, R.; Steffen, M.; Ansmann, M.; Osborn, K. D.; Cicak, K.; Oh, S.; Pappas, D. P.; Simmonds, R. W.; Yu, C. C. Decoherence in Josephson Qubits from Dielectric Loss. *Phys. Rev. Lett.* **2005**, 95 (21), 210503.
- (36) Quintana, C. M.; Megrant, A.; Chen, Z.; Dunsworth, A.; Chiaro, B.; Barends, R.; Campbell, B.; Chen, Y.; Hoi, I.-C.; Jeffrey, E.; Kelly, J.; Mutus, J. Y.; O'Malley, P. J. J; Neill, C.; Roushan, P.; Sank, D.; Vainsencher, A.; Wenner, J.; White, T. C.; Cleland, A. N.; Martinis, J. M. Characterization and Reduction of Microfabrication-Induced Decoherence in Superconducting Quantum Circuits. *Appl. Phys. Lett.* **2014**, *105* (6), 062601.
- (37) Ahn, Y.; Kim, J.; Ganorkar, S.; Kim, Y.-H.; Kim, S.-I. Thermal Annealing of Graphene to Remove Polymer Residues. *Mater. Express* **2016**, *6* (1), 69–76.
- (38) Ahmed, F.; Heo, S.; Yang, Z.; Ali, F.; Ra, C. H.; Lee, H.-I.; Taniguchi, T.; Hone, J.; Lee, B. H.; Yoo, W. J. Dielectric Dispersion and High Field Response of Multilayer Hexagonal Boron Nitride. *Adv. Funct. Mater.* **2018**, 28 (40), 1804235.
- (39) Lee, B. H.; Cho, Y. H.; Lee, H.; Lee, K.-D.; Kim, S. H.; Sung, M. M. High-Resolution Patterning of Aluminum Thin Films with a Water-Mediated Transfer Process. *Adv. Mater.* **2007**, *19* (13), 1714–1718.
- (40) Cueva, P.; Hovden, R.; Mundy, J. A.; Xin, H. L.; Muller, D. A. Data Processing for Atomic Resolution Electron Energy Loss Spectroscopy. *Microsc. Microanal.* **2012**, *18* (4), 667–675.